### Title
Redox Mediated Control of Electrochemical Potential in Liquid Cell Electron Microscopy




### Journal
Journal of the American Chemical Society, 143(31)

### ISSN
0002-7863



### Authors
Moreno-Hernandez, Ivan A
Crook, Michelle F
Ondry, Justin C
et al.



### Publication Date
2021-08-11

### DOI
10.1021/jacs.1c03906

Peer reviewed

# Redox Mediated Control of Electrochemical Potential in Liquid Cell Electron Microscopy

Ivan A. Moreno-Hernandez[1], Michelle F. Crook[1], Justin C. Ondry[1,3], and A. Paul Alivisatos[1-4*]

[1]Department of Chemistry, University of California, Berkeley, California 94720, United States

[2]Materials Sciences Division, Lawrence Berkeley National Laboratory, Berkeley, California 94720, United States

[3]Kavli Energy NanoScience Institute, Berkeley, California 94720, United States

[4]Department of Materials Science and Engineering, University of California, Berkeley, California 94720, United States

*Corresponding author. Email: paul.alivisatos@berkeley.edu

**ABSTRACT:** Liquid cell electron microscopy enables the study of nanoscale transformations in solvents with high spatial and temporal resolution, but for the technique to achieve its potential requires a new level of control over the reactivity caused by radical generation under electron beam irradiation. An understanding of how to control electron-solvent interactions is needed to further advance the study of structural dynamics for complex materials at the nanoscale. We developed an approach that scavenges radicals with redox species that form well-defined redox couples and control the electrochemical potential in situ. This approach enables the observation of electrochemical structural dynamics at near-atomic resolution with precise control of the liquid environment. Analysis of nanocrystal etching trajectories indicates that this approach can be generalized to several chemical systems. The ability to simultaneously observe heterogeneous reactions at near-atomic resolution and precisely control the electrochemical potential enables the fundamental study of complex nanoscale dynamics with unprecedented detail.

## INTRODUCTION

Liquid cell electron microscopy (LCEM) has enabled many discoveries related to nanoparticle dynamics, nanocrystal growth and etching trajectories, and three-dimensional atomic structure.[1-15] To date, researchers have had to adapt their experimental designs to the chemical environment created by the generation of radical species from electron-water interactions in liquid cells.[16-20] The addition of radical scavengers can decrease the concentration of radical species, but this approach has limited applicability due to the stoichiometric consumption of the scavenger species.[19] There is a pressing need to control the chemical environment within liquid cells under electron irradiation to observe reactions which can be reproduced *ex situ*, or to observe radical-sensitive materials. We aimed to identity a systematic approach to convert highly reactive radiolysis products into species which display well defined chemical reactivity, and ideally can be recycled over numerous reaction cycles. Electrochemical redox couples can provide stable and reversible reactivity regardless of the electrochemical potential used to drive their oxidation or reduction. For this reason, we hypothesized that addition of well-defined redox species into liquid cells will result in the scavenging of highly oxidative and reductive species through reaction with the redox couple.[21] This process will also result in the formation of well-defined redox couples, which will act as a "buffer" for the electrochemical environment during LCEM experiments due to the balanced oxidation and reduction kinetics of the redox additive. This should allow for rational control of the chemical environment in the liquid cell and enable the study of electrochemical reactions without the use of electrodes.

Electrochemical reactions have enabled several advances in the development of energy

storage technologies,[22] photonic devices,[23] nanocrystal synthesis methodologies,[24] and the electrochemical synthesis of commodity chemicals.[25] Structural dynamics that occur during electrochemical reactions are often probed with diffraction or spectroscopic techniques that provide ensemble information, or with microscopy techniques exhibiting microscale spatial resolution,[26-29] which limits mechanistic insight at the nanoscale. Although these techniques can be coupled with localized techniques for further insight,[30] methods to probe electrochemical structural dynamics at nanoscale or atomic-scale resolution remain limited. Efforts to control the electrochemical environment during LCEM experiments have focused on micro-fabricated silicon nitride liquid cells with electrodes for potential control.[4-5, 12] These approaches have substantially advanced the understanding of electrochemical reactions; however, this approach only allows control of the potential at the electrode/liquid interface, and highly reactive species generated in the liquid can still affect the reactivity observed.[4, 31] Chemical reactions are typically initiated in LCEM studies through electron-beam irradiation induced processes due to the strong interaction between the electron beam and the solvent.[1-2, 6, 16] These interactions lead to the formation of radicals that undergo reduction-oxidation reactions in the liquid phase and at solid-liquid interfaces.[2, 7-11, 32] Liquid cell studies have substantially improved our understanding of nanoscale phenomena; however, the technique is often limited to nanocrystals consisting of single elements, or material systems with large electrochemical potential differences, due to the limited control of the reactions initiated by electron-water interactions.

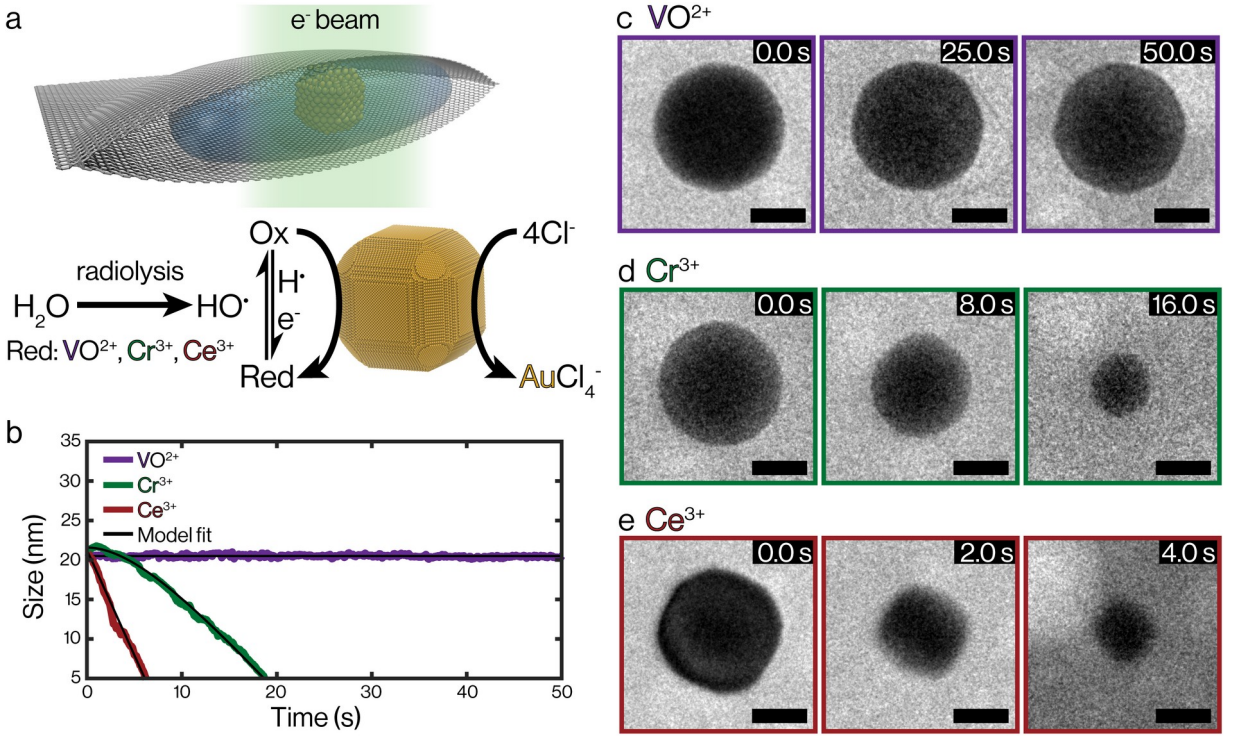


**Figure 1.** Mechanism and demonstration of redox additive approach used to control electrochemical reactions in graphene liquid cell electron microscopy. a) Electron beam generated radicals react with additives to form a well-defined redox couple, which directly etch nanocrystals at well-defined potentials. b) Volume trajectories of gold nanocrystals irradiated at 1200 $e^{-}$ $Å^{-2}$ $s^{-1}$ in graphene liquid cells containing 100 mM HCl and 10 mM V(IV), Cr(III), or Ce(III). c-e) TEM image time series with 10 nm scale bars collected during irradiation of graphene liquid cells containing 100 mM HCl and 10 mM V(IV), Cr(III), or Ce(III) respectively.

Here we demonstrate that redox additives that scavenge radicals and form redox couples *in situ* under irradiation can be used to control the electrochemical environment during LCEM studies of the dissolution of nanocrystals consisting of Pd, Au, or Pt (Fig. S1). Since these materials are known to etch at different potentials, they act as a chemical probe of the electrochemical environment within liquid cells.[32] Based on their known electrochemical potentials, we hypothesize that addition of **V(IV)** will result in a **V(IV)**/V(V) couple that will only etch Pd nanocrystals; **Cr(III)**/Cr(VI) should result in Pd and Au nanocrystal etching; the **Ce(III)**/Ce(IV) couple should enable etching studies of Pd, Au, and Pt.[33] Further details on the choice of redox

additives, experimental conditions, radiolysis modeling, and detailed nanocrystal etching trajectory analysis are provided in the Supporting information.

## EXPERIMENTAL SECTION

Pd, Au, and Pt nanocrystals were synthesized with aqueous colloidal techniques from metal chloride precursors, as described in the Supporting information. Graphene-coated gold TEM grids were prepared with a previously reported procedure.[34] Copper foil with 3-5 layers of CVD grown graphene (ACS Material) was washed in acetone three times at 50 °C for five minutes in order to remove residual polymer from the graphene surfaces. The graphene coated copper foil was allowed to air dry for one hour, and subsequently flattened with two glass microscope slides. Several gold TEM grids (300 Mesh Quantifoil, Holey Carbon, 1.3 µm hole diameter with 1.3 µm separation, Structure Probe, Inc.) were placed with the carbon-side down on the graphene-coated copper foil. Several µL of Isopropanol were added to the copper foil surface and allowed to dry for 2 hours to improve the physical adhesion between the graphene and gold TEM grids. The copper foil was floated in a solution of sodium persulfate (100 mg per mL) with the graphene side facing upward for at least 10 hours in order to etch the copper substrate. The graphene-coated gold TEM grids were retrieved from the sodium persulfate solution and washed with water three times and allowed to dry prior to use.

Graphene liquid cells were prepared by encapsulating a solution containing nanocrystals between two graphene-coated gold TEM grids. The solutions were prepared by adding 10 µL of a concentrated nanocrystal solution to 200 µL of a solution containing 100 mM HCl and 10 mM of $MgCl_2$ or a redox species. For solutions containing Mg(II), Ce(III), or Cr(III), solutions with 100 mM HCl were prepared prior to each experiment with Eu(III) acetate, $MgCl_2$, $CeCl_3$, or $CrCl_3$, respectively. A V(IV) solution was prepared by preparing a saturated solution of $V_2O_4$ in 2.0 M HCl and diluting with 100 mM HCl until a 10 mM V(IV) solution was obtained. The concentration of V(IV) was calibrated with a 10 mM $VOSO_4$ and 100 mM HCl solution using UV-Vis spectroscopy. Approximately 0.2 µL of the solution containing nanocrystals, 100 mM HCl, and 10 mM $MgCl_2$ or redox species was deposited with a micropipette onto the graphene-coated side of a gold TEM grid held by self-closing tweezers. A second graphene-coated TEM grid was cut in half with a blade. One half-grid was placed over the droplet on top of the first TEM grid. The droplet was allowed to dry for at least 10 minutes to form liquid pockets between the graphene-coated TEM grids.

Transmission electron microscope images were collected with an FEI Tecnai T20 S-Twin TEM operating at 200 kV with a $LaB_6$ filament. All videos were collected within 3 hours of forming the graphene liquid cells. Image time series were collected with a Gatan Rio 16 IS camera at 2048x2048 or 4096x4096 pixels at a nominal magnification of 97kx, resulting in a pixel resolution of 1.387 or 0.694 Å/pixel, respectively. The exposure time for each experiment was either 0.1 seconds or 0.2 seconds, resulting in a framerate of 10 fps or 5 fps, respectively. The electron beam dose was calibrated with a custom script as previously reported.[32] The electron beam dose rate was 1200 $e^- Å^{-2} s^{-1}$ for all experiments unless otherwise indicated. The electron beam was spread to a low dose while searching for a sample to prevent electron-beam induced reactions prior to imaging.

## RESULTS AND DISCUSSION

We observed the etching dynamics of single nanocrystals with graphene LCEM to understand the effect of redox additives on the electrochemical environment (Fig. 1, Supporting Movies 1 to 3). While our discussion initially focuses on the etching dynamics of gold, all nine redox additive and nanocrystal combinations were investigated. The addition of Cr(III) or Ce(III) results in complete etching of gold nanocrystals within a short time span, while the addition of V(IV) results in no substantial etching of gold nanocrystals. These results are consistent with electrochemical predictions from the thermodynamics and kinetics of gold dissolution (Fig. 1, Fig. S2).

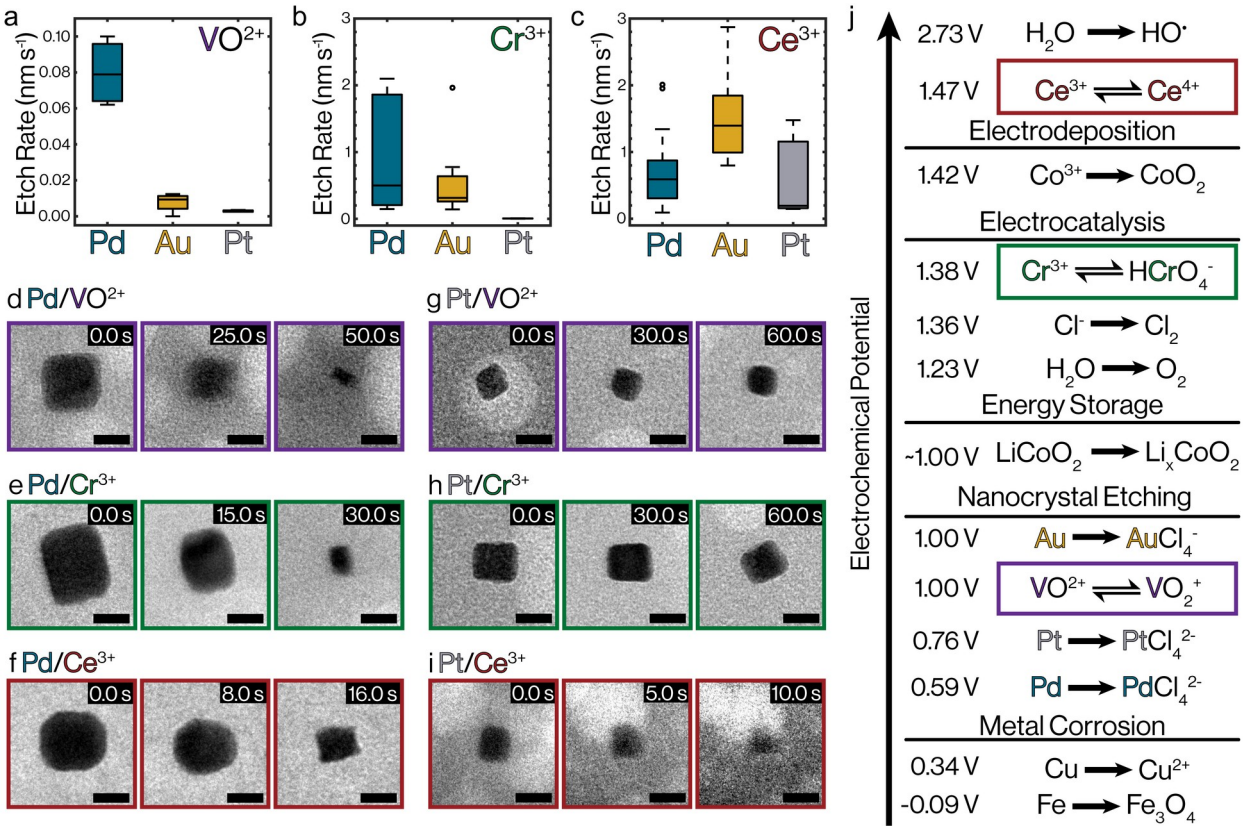


**Figure 2.** Summary of etching trajectories observed with V(IV), Cr(III), or Ce(III) redox additives. a-c) Statistics for etch rates of Pd, Au, and Pt nanocrystals in solutions containing 10 mM V(IV), Cr(III), or Ce(III) and 100 mM HCl. d-f) TEM image time series with 10 nm scale bars of Pd nanocrystals in graphene liquid cells containing V(IV), Cr(III), or Ce(III). g-i) TEM image time series with 10 nm scale bars of Pt nanocrystals in graphene liquid cells containing V(IV), Cr(III), or Ce(III). j) Electrochemical series of reactions studied or enabled by this study: electrochemical reactions including metal corrosion, nanocrystal etching, electrocatalysis, energy storage, and electrodeposition can be studied with the redox additives studied herein.

V(IV), Cr(III), and Ce(III) species were chosen because they form well-defined redox couples with their oxidized counterparts (Table S1), have electrochemical potentials that are relevant for several electrochemical reactions, and are known to undergo reduction-oxidation reactions with radiolysis species (Table S2).[21] We hypothesize that redox additives such as Ce(III) will be oxidized by electron-beam generated hydroxyl radicals to form Ce(IV). The Ce(IV) formed *in situ* will in turn be reduced by atomic hydrogen and solvated electrons back to Ce(III). Similar reaction pathways have been observed for V, Cr, and Ce species in water radiolysis studies (Table S2). We expect that this chemical cycle will lead to steady-state concentrations of Ce(III) and Ce(IV) that are in the same order of magnitude, which would establish an electrochemical potential within ± 50 mV of the standard electrochemical potential according to the Nernst equation. The redox couple formed *in situ* can react with materials in liquid cells via surface reactions. The V, Cr, and Ce redox couples span a potential range of 1.000 V to 1.466 V vs. the standard hydrogen electrode (SHE) (Table S1). Nanocrystals consisting of Pd, Au, or Pt dissolve in chloride containing solutions to form aqueous chloride complexes at well-defined thermodynamic electrochemical potentials (Table S1). However, observable dissolution also requires kinetic barriers to be overcome, which necessitates a potential above the thermodynamic dissolution potential. Cyclic voltammetry of metal electrodes in 100 mM HCl was used to determine that Pd, Au, and Pt require at least 0.72 V, 1.13 V, and 1.38 V vs. SHE, respectively, to dissolve at a rate of 0.05 nm $s^{-1}$ (Fig. S2). Thermodynamic analysis indicates that Pd, Au, and Pt nanocrystals will spontaneously dissolve when exposed to most redox couples studied herein (Table S3). However, analysis including the kinetic barriers associated with metal dissolution indicates that Au nanocrystals will be stable in V(V) containing solutions and Pt nanocrystals will be stable in V(V) and Cr(VI) containing solutions (Fig. S2, Table S4). Figure 1 shows the etching trajectories of truncated gold nanocubes in the presence of 10 mM V(IV), Cr(III), or Ce(III) and 100 mM HCl. The addition of V(IV) results in no substantial etching of gold nanocrystals for most experiments (Fig. 1B, 1C). Vanadium has multiple stable oxidation states,

but it is expected that reactions with radicals will lead to the partial formation of V(V) due to the oxidizing environment within graphene liquid cells (Table S2) [32]. The V(IV)/V(V) redox couple has a standard potential of 1.00 V vs. SHE, which is not sufficient to overcome kinetic barriers for gold dissolution.

Quantitative models were developed to understand the observed etching trajectories (see Supporting information). The etching trajectories can be modeled by the time-dependent generation of an oxidant species in the liquid phase, and a surface-limited reaction between the oxidant species and the nanocrystal at the solid-liquid interface. The model results in two parameters that can be fit to an etching trajectory: the etch rate of the nanocrystal (nm $s^{-1}$), and the generation rate of the oxidant ($s^{-1}$). Figure 1b indicates that the gold etching trajectories observed with V(IV), Cr(III), and Ce(III) additives could be accurately described by this model.

A homogeneous chemical reaction network model that simulates the effect of electron-water interactions and Ce(III) additives was developed to understand the influence of redox additives on the electrochemical environment of graphene liquid cells under electron irradiation.[16] The interactions between the Ce(III)/Ce(IV) redox couple and radiolysis species are well understood from pulse radiolysis experiments (Table S2).[21] Simulations indicate that radical species reach a steady-state concentration in less than $10^{-3}$ s, and that the addition of Ce(III) results in a decrease in the steady-state concentration of radical species due to scavenging (Fig. S4). The radical-scavenging effect of Ce(III) additives can be complemented by radical scavenging with $Cl^-$, which leads to the formation of $Cl_2$, $Cl_2^-$, and $Cl_3^-$ (Fig. S4). We simulated the effect of electron beam dose and initial Ce(III) concentration for 10,201 dose-concentration conditions without chloride ions present (Fig. S5) and with 100 mM chloride present (Fig. S6). In all cases an increase in the electron beam dose results in an increase of radicals. However, the addition of Ce(III) continuously decreases the steady-state concentration of atomic hydrogen and hydroxyl radicals at a fixed dose. At 100 mM Ce(III) without chloride present the concentration of hydroxyl radicals decreases by 83.6 – 99.5% due to scavenging for electron beam doses between 1 and 1,000 $e^-$ $Å^{-2}$ $s^{-1}$. The concentration of Ce(IV) exhibits a dose-insensitive region at electron doses between 1 and 10 $e^-$ $Å^{-2}$ $s^{-1}$, and at electron doses above 100 $e^-$ $Å^{-2}$ $s^{-1}$ for Ce concentrations below 50 mM (Fig. S5). For simulations containing 100 mM chloride, the effect of radical scavenging by Ce is less pronounced due to scavenging by chloride, which results in the net production of $Cl_3^-$ (Fig. S6). Scavenging of radicals by chloride results in a lower steady-state concentration of Ce(IV) (Fig. S6). However, chloride scavenging also results a wider region of dose insensitivity for the steady-state Ce(IV) concentration, which extends from 1 – 1,000 $e^-$ $Å^{-2}$ $s^{-1}$ for Ce(IV) concentrations from 1 to 100 mM (Fig. S6). The results of this quantitative chemical network model are consistent with the assumptions made to derive the model used to understand the etching trajectories of the nanocrystals. These results indicate that redox additives can act as a “buffer” to set the electrochemical potential through redox chemistry during LCEM experiments, similar to the use of acid-base buffers to set the pH through acid-base chemistry. An accurate model of electron-water interactions with V(IV) or Cr(III) redox species would be more complex due to the multiple reaction pathways of these species (Table S2), however, the Ce radiolysis model indicates the general reaction pathways that enable redox additives to control the electrochemical environment during LCEM experiments.

Further analysis of etching trajectories for Pd, Au, and Pt nanocrystals in V(IV), Cr(III), or Ce(III) containing liquid cells indicates that for all nanocrystal and redox additive combinations the etching behavior is consistent with the electrochemical potential of the redox couple (Fig. 2). The absolute value of the etch rate for all conditions studied depends on several variables such as the homogeneous reaction rates of the redox couples and the reaction kinetics at the nanocrystal surface. This prevents detailed comparisons of the absolute etch rates observed between different redox couple-nanocrystal combinations, however, the absence of etching in particular cases is indicative of potential control within graphene liquid cells. The control of electrochemical reactions with V(IV), Cr(III), and Ce(III) species enables the nanoscale structural dynamics of several electrochemical reactions to be studied at precisely controlled electrochemical potentials, including the corrosion of structural and electrical metals, the synthesis or dissolution of multi-metallic nanocrystals, the electrochemical synthesis of commodity chemicals, the energy storage reactions of battery materials, and the deposition of materials (Fig. 2j).

Control of the electrochemical environment in graphene liquid cells was further verified by observing the etching trajectories of nanocrystal mixtures (Fig. 3, Supporting Movies 4 and 5). Pd, Au, and Pt nanocrystals were synthesized with different shape and size distributions, allowing the elemental identification of individual nanocrystals from their initial size and shape (Fig. S1). Analysis of the kinetic potential associated with metal dissolution indicates that selective Pd nanocrystal dissolution should be observed for Pd-Au mixtures in V(IV) containing liquid cells, and selective Au nanocrystal dissolution should be observed for Au-Pt mixtures in Cr(III) containing liquid cells (Table S4). Graphene liquid

cells were prepared with V(IV) and Pd-Au nanocrystal mixtures from Pd and Au nanocrystal samples exhibiting a size distribution of 17.7 ± 2.8 nm and 22.4 ± 2.0 nm, respectively (Fig. S1). The etch rate of Pd in Pd-Au nanocrystal mixtures was 0.09 nm $s^{-1}$, while Au did not etch (Fig. 3b). Graphene liquid cells were prepared with Cr(III) and Au-Pt mixtures from Au and Pt nanocrystal samples exhibiting a size distribution of 22.4 ± 2.0 nm and 8.6 ± 1.3 nm, respectively (Fig. S1). The etch rate of Au in this environment was 0.24 nm $s^{-1}$, while Pt did not etch (Fig. 3e). The etch rates of Pd and Au nanocrystals in Pd-Au or Au-Pt mixtures are consistent with the etch rates observed for individual nanocrystals (Fig. 2-3). The results indicate that V(IV) and Cr(III) redox additives can be used to precisely control the electrochemical environment within graphene liquid cells and enable the selective oxidation of certain materials in complex material mixtures.

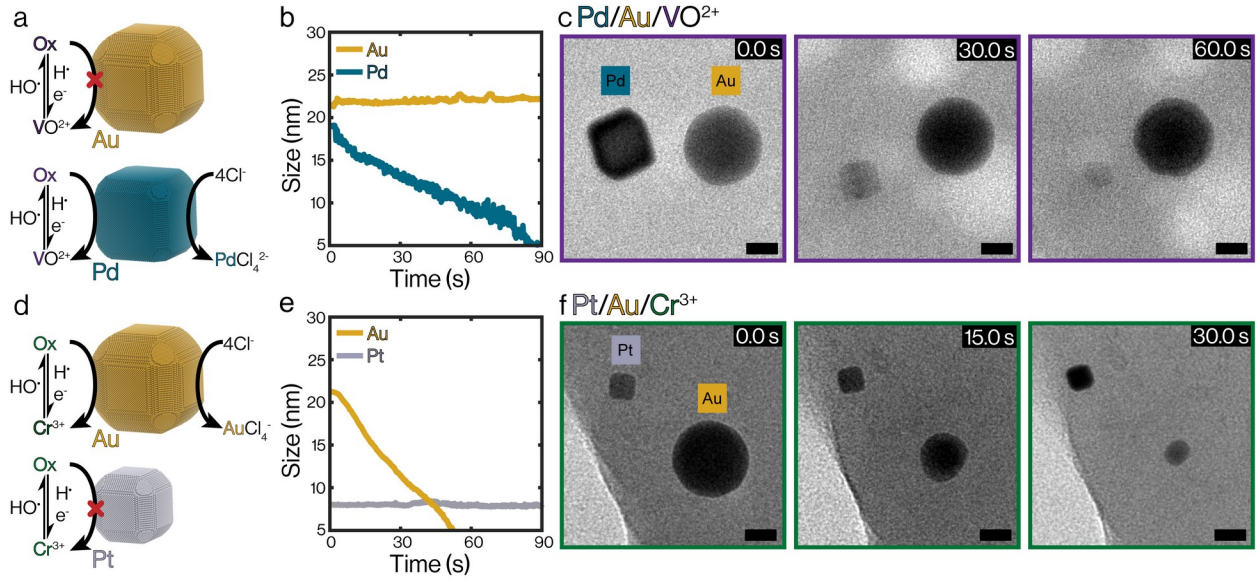


**Figure 3.** Selective etching of nanocrystal mixtures with redox additives. a) Schematic of reaction mechanism that leads to selective etching of Pd in Pd-Au nanocrystal mixtures for graphene liquid cells containing V(IV). b) Volume trajectory of a Pd and Au nanocrystal pair irradiated at 1200 $e^{-}$ $Å^{-2}$ $s^{-1}$ in a graphene liquid cell containing 10 mM V(IV) and 100 mM HCl. c) TEM image time series with 10 nm scale bars of a Pd and Au nanocrystal pair in a V(IV) containing graphene liquid cell. d) Schematic of reaction mechanism that leads to selective etching of Au in Au-Pt nanocrystal mixtures for graphene liquid cells containing Cr(III). e) Volume trajectory of a pair of Au and Pt nanocrystals irradiated at 1200 $e^{-}$ $Å^{-2}$ $s^{-1}$ in a graphene liquid cell containing 10 mM Cr(III) and 100 mM HCl. f) TEM image time series with 10 nm scale bars of a pair of Au and Pt nanocrystals in a Cr(III) containing graphene liquid cell.

Hollow nanoparticles are an important class of structures with applications in catalysis, energy storage, medicine, and plasmonics.[35-37] Hollow structures can be formed by selectively etching the core of a core@shell nanocrystal with a redox species, which allows precise control of the resulting nanocage.[35] LCEM can be used to directly observe the formation of hollow structures, however, precise control of the electrochemical potential is required to selectively etch cores in certain structures, such as Pd@Au nanocrystals.[11] We etch Pd in Pd@Au core-shell nanocubes in V(IV) containing graphene liquid cells to understand the formation of Au nanocages and to highlight the electrochemical control enabled by the redox additive approach (Fig. 4, Supporting Movie 6). V(V) has an intermediate potential between Pd and Au, thus we would expect that only the Pd would etch, leaving a hollow gold shell in solution. Palladium nanocubes were coated with a gold shell that was 3.7 ± 0.5 nm thick (Fig. 4a, Fig. S7). The shell growth resulted in defects at the nanocrystal edges, which allowed the liquid to directly contact the underlying Pd nanocube (Fig. 4). The nanocrystal was observed to etch at the nanocrystal edges preferentially. Pd nanocrystals in V(IV) containing solutions substantially etched along the (100) crystallographic orientation (Fig. 2d). The Pd@Au nanocrystals did not etch along the (100) crystallographic orientation, indicating that regions uniformly coated with Au were stable (Fig. 4c). The nanocrystal length along the (110) orientation decreased from 44.7 nm to 32.3 nm over 40 seconds, corresponding to a length decrease of 12.4 nm, and a stable nanocrystal length of 31.8 nm was observed after 60 seconds (Fig. 4c). Pd nanocrystals exhibited an etch rate of 0.06 - 0.10 nm $s^{-1}$ for the first and third quartiles, which corresponds to a decrease in length along the (110) orientation by 6.8 – 11.3 nm over 40 seconds (Fig. 2). The length decrease

observed for Pd@Au nanocrystals is within the fourth quartile observed for individual Pd nanocrystals. Similar experiments were conducted with Pd@Au core-shell nanocubes synthesized with different amounts of gold, and these studies indicate that thinner gold shells lead to complete nanocrystal dissolution and thicker gold shells protect the nanocrystal from etching, while nanocrystals with a gold shell thickness of 3.7 ± 0.5 nm exhibit stable shell dimensions after 60 s (Fig. S8). The results indicate that for Pd@Au nanocrystals with an intermediate Au thickness the Pd core was preferentially etched. Previous studies have investigated the etching dynamics of Pd@Au nanocrystals with an Fe(III) chemical additive, which allows preferential etching of Pd in Pd@Au nanocrystals.[11] However, the Fe(III) additive results in complete dissolution of both Pd and Au over time.[11] In this work V(IV) additives create a milder chemical environment compared to Fe(III) as indicated by the stability of 3.7 nm Au shells (Fig. 4a), compared to the complete dissolution of 21 – 38 nm Au shells observed previously with Fe(III).[11] Pd@Au nanocrystals coated with a uniform Au shell did not etch in graphene liquid cells containing V(IV) (Fig. S8b), further indicating that V(IV) results in a milder environment compared to Fe(III). The etching observed along the (110) orientation is attributed to decreased stability of Au due to the presence of structural defects near nanocrystals edges (Fig 4a). Additionally, the stability of hollow nanostructures can be affected by mechanical properties in addition to chemical properties.[35] It is expected that precise control of these structural defects would lead to improved control of hollow nanostructure formation.

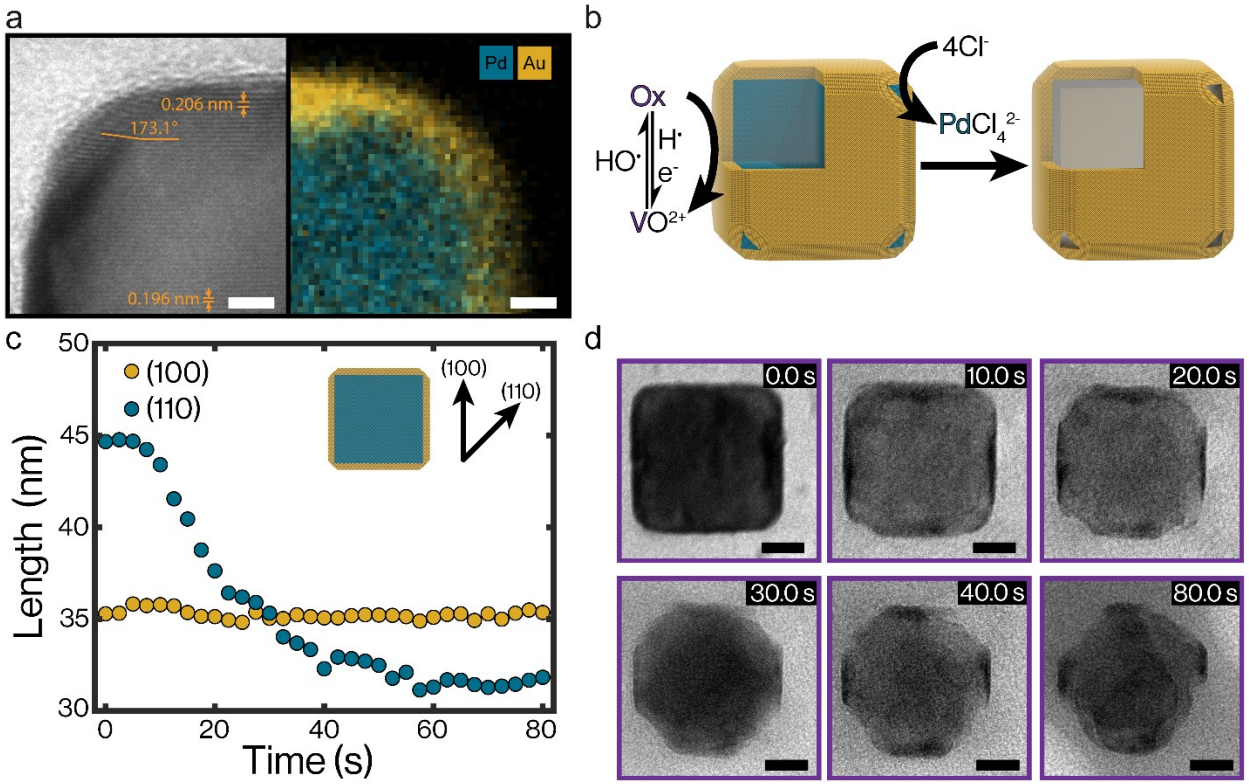


**Figure 4.** Selective Pd etching of Pd@Au nanocrystal with a V redox additive. a) High-resolution TEM image of a Pd@Au core-shell nanoparticle and corresponding elemental map with 2 nm scale bars. b) Schematic of selective Pd dissolution of Pd@Au nanocrystals: oxidized vanadium species can be reduced at the gold surface, allowing electron transfer to the Pd core and subsequent dissolution of Pd at sites exposed to the liquid phase. c) Nanocrystal length along the (100) and (110) crystal orientations of a Pd@Au core-shell nanocrystal dissolving in a V(IV) containing liquid cell irradiated at 1200 $e^{-}$ $Å^{-2}$ $s^{-1}$. d) TEM image series with 10 nm scale bars of a Pd@Au core-shell nanocrystal dissolving in a V(IV) containing liquid cell.

## CONCLUSION

Our results indicate a general approach to obtain electrochemical control during LCEM experiments. Reduced species react with radical species generated during irradiation, and lead to the formation of well-defined redox couples that control the electrochemical environment within liquid cells. This approach was implemented with nine redox species/nanocrystal combinations, with all cases exhibiting etching behavior consistent with electrochemical principles. It is expected that this approach can be generalized to additional redox couples that enable the study of cathodic reactions such as nanocrystal growth or enable the control of reactivity in other liquid environments. Criteria to identify additional redox couples include the ability to dissolve and form

stable oxidized and reduced species, and the ability to reversibly form both oxidation states through reactions with radical species generated in-situ. This approach could also enable the study of sensitive materials by scavenging radicals to obtain an electrochemical environment that does not interact directly with the sample, and can be complemented with advanced liquid cell geometries or techniques.[38-39] For example, certain biological structures contain nucleosides that oxidize at potentials ranging from 1.29 – 1.70 V vs. NHE.[40] These structures could be studied with improved stability under LCEM conditions with redox additives such as V(IV) that establish an electrochemical potential below this range to prevent nucleoside oxidation. Additionally, photocatalytic semiconductors that exhibit a narrow potential range between operation and stability could be studied *in situ* with appropriate redox additives.[41] The ability to precisely control electron beam-solvent interactions during imaging will allow LCEM to become an invaluable technique to study nanoscale structural dynamics at near-atomic resolution.[31]

## ASSOCIATED CONTENT

### Supporting Information

The supporting information is available free of charge at

Supporting methods, chemicals, nanoparticle synthesis, electrochemical characterization, energy-dispersive x-ray spectroscopy mapping, image analysis, homogeneous radiolysis chemical reaction network model, nanocrystal etching trajectory model, supporting discussion, supporting figures S1 to S9, tables S1 to S5, supporting movies 1 to 7

## AUTHOR INFORMATION


### Corresponding Author

* A. Paul Alivisatos

Department of Chemistry, University of California, Berkeley, California 94720, United States

Materials Sciences Division, Lawrence Berkeley National Laboratory, Berkeley, California 94720, United States

Kavli Energy NanoScience Institute, Berkeley, California 94720, United States

Department of Materials Science and Engineering, University of California, Berkeley, California 94720, United States

Email: paul.alivisatos@berkeley.edu


### Author Contributions

The manuscript was written through contributions of all authors.

## ACKNOWLEDGMENT


This work was supported by the 'Photonics at Thermodynamic Limits' Energy Frontier Research Center funded by the U.S. Department of Energy (DOE), Office of Science, Office of Basic Energy Sciences, under award DE-SC0019140. Work at the Molecular Foundry was supported by the Office of Science, Office of Basic Energy Sciences, of the U.S. Department of Energy under Contract No. DE-AC02-05CH11231. M.F.C. gratefully acknowledges support from the National Science Foundation's Graduate Research Fellowship Program (NSF GRFP). J.C.O. gratefully acknowledges the support of the Kavli Philomathia Graduate Student Fellowship.


## REFERENCES


(1) Yuk, J. M.; Park, J.; Ercius, P.; Kim, K.; Hellebusch, D. J.; Crommie, M. F.; Lee, J. Y.; Zettl, A.; Alivisatos, A. P., High-Resolution EM of Colloidal Nanocrystal Growth Using Graphene Liquid Cells. *Science* **2012,** *336* (6077), 61-64.

(2) Ye, X.; Jones, M. R.; Frechette, L. B.; Chen, Q.; Powers, A. S.; Ercius, P.; Dunn, G.; Rotskoff, G. M.; Nguyen, S. C.; Adiga, V. P.; Zettl, A.; Rabani, E.; Geissler, P. L.; Alivisatos, A. P., Single-particle mapping of nonequilibrium nanocrystal transformations. *Science* **2016,** *354* (6314), 874-877.

(3) de Jonge, N.; Ross, F. M., Electron microscopy of specimens in liquid. *Nat. Nanotech.* **2011,** *6* (11), 695-704.

(4) Hodnik, N.; Dehm, G.; Mayrhofer, K. J., Importance and Challenges of Electrochemical in Situ Liquid Cell Electron Microscopy for Energy Conversion Research. *Acc. Chem. Res.* **2016,** *49* (9), 2015-22.

(5) Ross, F. M., Opportunities and challenges in liquid cell electron microscopy. *Science* **2015,** *350* (6267), aaa9886.

(6) Yang, J.; Koo, J.; Kim, S.; Jeon, S.; Choi, B. K.; Kwon, S.; Kim, J.; Kim, B. H.; Lee, W. C.; Lee, W. B.; Lee, H.; Hyeon, T.; Ercius, P.; Park, J., Amorphous-Phase-Mediated Crystallization of Ni Nanocrystals Revealed by High-Resolution Liquid-Phase Electron Microscopy. *J. Am. Chem. Soc.* **2019,** *141* (2), 763-768.

(7) Park, J. H.; Schneider, N. M.; Grogan, J. M.; Reuter, M. C.; Bau, H. H.; Kodambaka, S.; Ross, F. M., Control of Electron Beam-Induced Au Nanocrystal Growth Kinetics through Solution Chemistry. *Nano Lett.* **2015,** *15* (8), 5314-20.

(8) Loh, N. D.; Sen, S.; Bosman, M.; Tan, S. F.; Zhong, J.; Nijhuis, C. A.; Kral, P.; Matsudaira, P.; Mirsaidov, U., Multistep nucleation of nanocrystals in aqueous solution. *Nat. Chem.* **2017,** *9* (1), 77-82.

(9) Yang, J.; Zeng, Z.; Kang, J.; Betzler, S.; Czarnik, C.; Zhang, X.; Ophus, C.; Yu, C.; Bustillo, K.; Pan, M.; Qiu, J.; Wang, L. W.; Zheng, H., Formation of two-dimensional transition metal oxide nanosheets with nanoparticles as intermediates. *Nat. Mater.* **2019,** *18* (9), 970-976.

(10) Zheng, H.; Smith, R. K.; Jun, Y.-w.; Kisielowski, C.; Dahmen, U.; Alivisatos, A. P., Observation of Single Colloidal Platinum Nanocrystal Growth Trajectories. *Science* **2009,** *324* (5932), 1309-1312.

(11) Chen, L.; Leonardi, A.; Chen, J.; Cao, M.; Li, N.; Su, D.; Zhang, Q.; Engel, M.; Ye, X., Imaging the kinetics of anisotropic dissolution of bimetallic core-

shell nanocubes using graphene liquid cells. *Nat. Commun.* **2020,** *11* (1), 3041.
(12) Tan, S. F.; Chee, S. W.; Baraissov, Z.; Jin, H.; Tan, T. L.; Mirsaidov, U., Intermediate Structures of Pt-Ni Nanoparticles during Selective Chemical and Electrochemical Etching. *J. Phys. Chem. Lett.* **2019,** *10* (20), 6090-6096.
(13) Jeon, S.; Heo, T.; Hwang, S.-Y.; Ciston, J.; Bustillo, K. C.; Reed, B. W.; Ham, J.; Kang, S.; Kim, S.; Lim, J.; Lim, K.; Kim, J. S.; Kang, M.-H.; Bloom, R. S.; Hong, S.; Kim, K.; Zettl, A.; Kim, W. Y.; Ercius, P.; Park, J.; Lee, W. C., Reversible disorder-order transitions in atomic crystal nucleation. *Science* **2021,** *371* (6528), 498-503.
(14) Tan, S. F.; Chee, S. W.; Baraissov, Z.; Jin, H.; Tan, T. L.; Mirsaidov, U., Real-Time Imaging of Nanoscale Redox Reactions over Bimetallic Nanoparticles. *Adv. Funct. Mater.* **2019,** *29* (37).
(15) Woehl, T. J., Metal Nanocrystal Formation during Liquid Phase Transmission Electron Microscopy: Thermodynamics and Kinetics of Precursor Conversion, Nucleation, and Growth. *Chem. Mater.* **2020,** *32* (18), 7569-7581.
(16) Schneider, N. M.; Norton, M. M.; Mendel, B. J.; Grogan, J. M.; Ross, F. M.; Bau, H. H., Electron−Water Interactions and Implications for Liquid Cell Electron Microscopy. *J. Phys. Chem. C* **2014,** *118*, 22373-22382.
(17) El Omar, A. K.; Schmidhammer, U.; Rousseau, B.; LaVerne, J.; Mostafavi, M., Competition Reactions of $H_2O^{\bullet+}$ Radical in Concentrated $Cl^-$ Aqueous Solutions: Picosecond Pulse Radiolysis Study. *J. Phys. Chem. A* **2012,** *116* (47), 11509-18.
(18) Ambrožič, B.; Prašnikar, A.; Hodnik, N.; Kostevšek, N.; Likozar, B.; Rožman, K. Ž.; Šturm, S., Controlling the radical-induced redox chemistry inside a liquid-cell TEM. *Chem. Sci.* **2019,** *10*, 8735-8743.
(19) Cho, H.; Jones, M. R.; Nguyen, S. C.; Hauwiller, M. R.; Zettl, A.; Alivisatos, A. P., The Use of Graphene and Its Derivatives for Liquid-Phase Transmission Electron Microscopy of Radiation-Sensitive Specimens. *Nano Lett.* **2017,** *17* (1), 414-420.
(20) Woehl, T. J.; Abellan, P., Defining the radiation chemistry during liquid cell electron microscopy to enable visualization of nanomaterial growth and degradation dynamics. *J. Microsc.* **2017,** *265* (2), 135-147.
(21) Buxton, G. V.; Greenstock, C. L.; Helman, W. P.; Ross, A. B., Critical Review of Rate Constants for Reactions of Hydrated Electrons, Hydrogen Atoms and Hydroxyl Radicals (·OH/·$O^-$) in Aqueous Solution. *J. Phys. Chem. Ref. Data* **1988,** *17* (2), 513-886.
(22) Larcher, D.; Tarascon, J. M., Towards greener and more sustainable batteries for electrical energy storage. *Nat. Chem.* **2015,** *7* (1), 19-29.
(23) van de Groep, J.; Song, J.-H.; Celano, U.; Li, Q.; Kik, P. G.; Brongersma, M. L., Exciton resonance tuning of an atomically thin lens. *Nat. Photonics* **2020,** *14* (7), 426-430.
(24) Tian, N.; Zhou, Z.-Y.; Sun, S.-G.; Ding, Y.; Wang, Z. L., Synthesis of Tetrahexahedral Platinum Nanocrystals with High-Index Facets and High Electro-Oxidation Activity. *Science* **2007,** *316* (5825), 732-735.
(25) De Luna, P.; Hahn, C.; Higgins, D.; Jaffer, S. A.; Jaramillo, T. F.; Sargent, E. H., What would it take for renewably powered electrosynthesis to displace petrochemical processes? *Science* **2019,** *364* (6438).
(26) Timoshenko, J.; Roldan Cuenya, B., In Situ/Operando Electrocatalyst Characterization by X-ray Absorption Spectroscopy. *Chem. Rev.* **2021,** *121* (2), 882-961.
(27) Lin, F.; Liu, Y.; Yu, X.; Cheng, L.; Singer, A.; Shpyrko, O. G.; Xin, H. L.; Tamura, N.; Tian, C.; Weng, T. C.; Yang, X. Q.; Meng, Y. S.; Nordlund, D.; Yang, W.; Doeff, M. M., Synchrotron X-ray Analytical Techniques for Studying Materials Electrochemistry in Rechargeable Batteries. *Chem. Rev.* **2017,** *117* (21), 13123-13186.
(28) Lin, T. C.; Dawson, A.; King, S. C.; Yan, Y.; Ashby, D. S.; Mazzetti, J. A.; Dunn, B. S.; Weker, J. N.; Tolbert, S. H., Understanding Stabilization in Nanoporous Intermetallic Alloy Anodes for Li-Ion Batteries Using Operando Transmission X-ray Microscopy. *ACS Nano* **2020,** *14* (11), 14820-14830.
(29) Lim, J.; Li, Y.; Alsem, D. H.; So, H.; Lee, S. C.; Bai, P.; Cogswell, D. A.; Liu, X.; Jin, N.; Yu, Y.-s.; Salmon, N. J.; Shapiro, D. A.; Bazant, M. Z.; Tyliszczak, T.; Chueh, W. C., Origin and hysteresis of lithium compositional spatiodynamics within battery primary particles. *Science* **2016,** *353* (6299), 566-571.
(30) Kurouski, D.; Mattei, M.; Van Duyne, R. P., Probing Redox Reactions at the Nanoscale with Electrochemical Tip-Enhanced Raman Spectroscopy. *Nano Lett.* **2015,** *15* (12), 7956-62.
(31) de Jonge, N.; Houben, L.; Dunin-Borkowski, R. E.; Ross, F. M., Resolution and aberration correction in liquid cell transmission electron microscopy. *Nat. Rev. Mater.* **2018,** *4* (1), 61-78.
(32) Hauwiller, M. R.; Ondry, J. C.; Chan, C. M.; Khandekar, P.; Yu, J.; Alivisatos, A. P., Gold Nanocrystal Etching as a Means of Probing the Dynamic Chemical Environment in Graphene Liquid Cell Electron Microscopy. *J. Am. Chem. Soc.* **2019,** *141* (10), 4428-4437.
(33) Bard, A. J.; Faulkner, L. R., *Electrochemical Methods: Fundamentals and Applications*. Wiley New York: 2001; Vol. 2.
(34) Hauwiller, M. R.; Ondry, J. C.; Alivisatos, A. P., Using Graphene Liquid Cell Transmission Electron Microscopy to Study in Situ Nanocrystal Etching. *J. Vis. Exp.* **2018,** (135), e57665.
(35) Zhang, L.; Roling, L. T.; Wang, X.; Vara, M.; Chi, M.; Liu, J.; Choi, S.-I.; Park, J.; Herron, J. A.; Xie, Z.; Mavrikakis, M.; Xia, Y., Platinum-based nanocages with subnanometer-thick walls and well-defined, controllable facets. *Science* **2015,** *349* (6246), 412-416.
(36) Park, J.; Kwon, T.; Kim, J.; Jin, H.; Kim, H. Y.; Kim, B.; Joo, S. H.; Lee, K., Hollow nanoparticles as emerging electrocatalysts for renewable energy conversion reactions. *Chem. Soc. Rev.* **2018,** *47* (22), 8173-8202.
(37) Wang, X.; Feng, J.; Bai, Y.; Zhang, Q.; Yin, Y., Synthesis, Properties, and Applications of Hollow Micro-/Nanostructures. *Chem. Rev.* **2016,** *116* (18), 10983-1060.
(38) Park, J.; Koo, K.; Noh, N.; Chang, J. H.; Cheong, J. Y.; Dae, K. S.; Park, J. S.; Ji, S.; Kim, I. D.; Yuk, J. M., Graphene Liquid Cell Electron Microscopy: Progress, Applications, and Perspectives. *ACS Nano* **2021,** *15* (1), 288-308.

(39) Dunn, G.; Adiga, V. P.; Pham, T.; Bryant, C.; Horton-Bailey, D. J.; Belling, J. N.; LaFrance, B.; Jackson, J. A.; Barzegar, H. R.; Yuk, J. M.; Aloni, S.; Crommie, M. F.; Zettl, A., Graphene-Sealed Flow Cells for In Situ Transmission Electron Microscopy of Liquid Samples. *ACS Nano* **2020,** *14* (8), 9637-9643.
(40) Steenken, S.; Jovanovic, S. V., How Easily Oxidizable Is DNA? One-Electron Reduction Potentials of Adenosine and Guanosine Radicals in Aqueous Solution. *J. Am. Chem. Soc.* **1997,** *119* (3), 617-618.
(41) Chen, S.; Wang, L.-W., Thermodynamic Oxidation and Reduction Potentials of Photocatalytic Semiconductors in Aqueous Solution. *Chem. Mater.* **2012,** *24* (18), 3659-3666.

Table of Contents Image